

## Numerical simulations of the interaction of internal waves with a shelf break

S. K. Venayagamoorthy and O. B. Fringer

*Environmental Fluid Mechanics Laboratory, Department of Civil and Environmental Engineering, Stanford University, Stanford, California 94305-4020*

(Received 24 January 2006; accepted 19 June 2006; published online 17 July 2006)

The energetics of the interaction of internal gravity waves with a shelf break is investigated by means of high-resolution two-dimensional numerical simulations, with an emphasis on understanding the partitioning of the internal wave energy over the course of the interaction process and the subsequent dynamics of the onshore propagating internal waves. Some of the energy is dissipated as a result of the instabilities associated with breaking, while the remaining energy is either reflected back away from or transmitted onto the shelf. We employ an analysis of the distribution of the energy flux across the shelf break taking into account the contributions from nonhydrostatic as well as nonlinear effects to quantify the percentage of energy flux that is transmitted onto the shelf, as well as the percentages of reflected and dissipated energy fluxes, from an incoming wave field. For a given frequency of an incoming wave, we vary the amplitude of the wave to vary the incident energy flux, and we simulate conditions ranging from subcritical to supercritical slopes by varying the topographic slope angle. The results show that the cumulative transmitted energy flux is a strong function of the ratio of the topographic slope  $\gamma$ , to wave characteristic slope  $s$ , while the reflected energy flux is a strong function of both  $\gamma/s$  as well as the nonlinearity. The energy flux calculations indicate that the internal boluses that form as a result of the interaction of the incident wave with the slope are very energetic, especially for critical to supercritical slopes. These nonlinear internal waves are plausible candidates for effectively transporting mass onshore, not withstanding their contribution to diapycnal mixing as well.

© 2006 American Institute of Physics. [DOI: 10.1063/1.2221863]

### I. INTRODUCTION

Understanding the interaction of internal waves with topography is a pressing problem in oceanography. The interaction of internal waves with bottom features such as continental slopes, seamounts, and ridges in the ocean can lead to instabilities and wave breaking, which results in strong mixing close to the boundaries. It has been hypothesized that, in conjunction with mixing in the interior of the ocean, this is a plausible mechanism through which oceanic mixing is sustained (Munk and Wunsch<sup>1</sup>). Indeed, many field experiments have provided evidence to suggest that the oceanic internal wave field has a considerable amount of energy to ignite intense diapycnal mixing near the boundaries (Ledwell *et al.*,<sup>2</sup> Polzin *et al.*,<sup>3</sup> Kunze and Toole<sup>4</sup>), supporting the conjecture that the internal wave field is the only serious candidate for supply of energy for vertical mixing in the open ocean.

Recent *in situ* and remote-sensing observations clearly show the presence of nonlinear internal waves (hereinafter referred to as NLIWs) in marginal seas and coastal waters (Ostrovsky and Stepanyants;<sup>5</sup> Apel *et al.*,<sup>6</sup> Sandstrom and Oakey,<sup>7</sup> Klymak and Moum,<sup>8</sup> Hosegood *et al.*,<sup>9</sup> Scotti and Pineda,<sup>10</sup> Carter *et al.*<sup>11</sup>). There are a number of ways through which these waves can be generated such as interaction of long, first-mode internal tides with bottom topography, lee-wave release, and wave-wave interactions. However, very little is known about the energetics and structure

of these highly nonlinear internal waves and their ultimate fate, especially as they propagate onshore into shoaling regions (Vlasenko and Hutter<sup>12</sup>). These NLIWs are likely to be an integral link in the pathway between the internal wave energy field in the deep ocean and turbulent dissipation. Therefore, understanding the dynamics of these NLIWs has far-reaching implications for numerous applications in the coastal environment.

Theoretical descriptions of NLIWs are based almost universally on weakly nonlinear formulations based on asymptotic expansions (e.g., Thorpe,<sup>13</sup> Dauxois and Young,<sup>14</sup> as well as the Korteweg–de Vries equation). These approaches do not apply to large-amplitude overturning or breaking internal waves. Several laboratory and numerical studies have been performed on the interaction of internal waves with submarine topography. In particular, when an internal wave-field in a continuously stratified fluid encounters topography in which the slope matches the angle of the internal wave group velocity, breaking occurs as a result of focusing of internal wave energy along the slope (e.g., see Phillips<sup>15</sup>). This problem has been studied via direct numerical simulations by Slinn and Riley<sup>16</sup> and Javam *et al.*<sup>17</sup> and in earlier laboratory experiments by Cacchione and Wunsch,<sup>18</sup> Ivey and Nokes,<sup>19</sup> and Ivey *et al.*<sup>20</sup> These authors have found that the most significant effect of the breaking process is the development of a nonlinear bolus (a vortex of dense fluid) that moves up-slope, mixing fluid and dissipating energy in the process. At the field scale, Legg and

Aderoff<sup>21</sup> studied the interaction of the internal tide with concave and convex slopes, and showed that both slope types induce a similar amount of turbulence and mixing as well as the generation of up-slope-propagating boluses. Field scale measurements (Stanton and Ostrovsky,<sup>22</sup> Carter *et al.*<sup>11</sup>) associate enhanced turbulence levels with nonlinear internal waves. For example, Klymak and Moum<sup>8</sup> have observed (probably for the first time) a sequence of three nonlinear internal solitary waves of elevation over Oregon's continental shelf and raise some unanswered questions with regard to how they form, how far onshore they propagate, and an understanding of their eventual fate.

A key component in gaining improved understanding of NLIWs deals with their energy flux budget. For a small-amplitude linear wave with a wave characteristic slope  $s$  encountering a shelf break with topographic slope  $\gamma < s$ , most of the energy is transmitted (forward-reflected), and the slope is said to be subcritical. The converse is true for a supercritical slope ( $\gamma > s$ ) with large amplitude where most of the wave energy is reflected backwards from the topography. A critical slope is obtained when  $\gamma = s$ , for which the reflected wave is parallel to the topography and focusing of wave energy takes place. This leads to enhanced dissipation and mixing in the bottom boundary layer. The dynamics is well understood for linear and weakly nonlinear waves (Phillips,<sup>15</sup> Craig,<sup>23</sup> Thorpe,<sup>13</sup> Dauxois and Young<sup>14</sup>); however, the role of the slope of the topography is neither fully recognized nor completely understood in the strongly nonlinear case. Hence, a fundamental understanding of the energy flux distribution across a shelf break for NLIWs is warranted. To this end, our study aims toward a better understanding of the energy flux distribution for NLIWs across an idealized shelf break using laboratory-scale numerical simulations.

In this paper, we present results from high-resolution two-dimensional numerical simulations of the interaction of a first-mode internal wave field with an idealized shelf break. Our emphasis is to obtain an understanding of the partitioning of the internal wave energy over the course of the interaction process and to gain insight into the dynamics of the onshore propagating internal boluses that form as a result of the interaction of nonlinear internal waves with topography. The numerical method and simulation setup is discussed in Sec. II. The energetics of these waves are discussed in Sec. III and conclusions are given in Sec. IV.

## II. NUMERICAL METHOD AND PROBLEM CONFIGURATION

The Navier-Stokes equations with the Boussinesq approximation and with constant kinematic viscosity are given by

$$\frac{\partial \mathbf{u}}{\partial t} + \mathbf{u} \cdot \nabla \mathbf{u} = -\frac{1}{\rho_0} \nabla p + \nu \nabla^2 \mathbf{u} - \frac{g}{\rho_0} \rho \mathbf{k}, \quad (1)$$

subject to the continuity constraint  $\nabla \cdot \mathbf{u} = 0$ , where  $\nu$  is the (constant) kinematic viscosity. The density field evolves according to

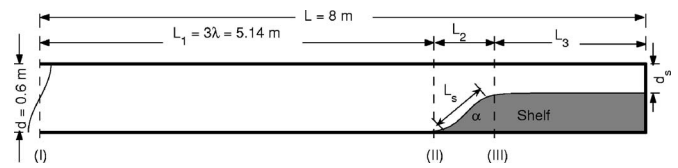


FIG. 1. Schematic of the computational setup that forms the domain for the present simulations. The buoyancy frequency is fixed at  $N=0.57$  rad/s, corresponding to a density difference of  $\Delta\rho/\rho_0=2\%$  over the depth. The frequency of the incoming mode-1 internal wave is fixed at  $\omega=0.33$  rad/s and  $\lambda=2\pi/k=1.713$  m. Lines (I), (II), and (III) represent the transects used to compute the energy flux in Sec. III B. The horizontal length  $L_2$  of the slope and the on-shelf water depth  $d_s$  are varied to obtain a range of slope angles  $\alpha$  such that the slope length  $L_s=[L_2^2+(d-d_s)^2]^{1/2}=d=0.6$  m is kept constant for all runs. The on-shelf length  $L_3$  is varied such that the overall length is  $L=8$  m.

$$\frac{\partial \rho}{\partial t} + \nabla \cdot (\rho \mathbf{u}) = \kappa \nabla^2 \rho, \quad (2)$$

where  $\kappa$  is the (constant) thermal diffusivity. Equations (1) and (2) are computed with the large-eddy simulation code developed by Fringer and Street<sup>24</sup> in the two-dimensional domain shown in Fig. 1. This code employs the fractional-step method of Zang *et al.*<sup>25</sup> to solve the Navier-Stokes and scalar transport equations presented in Eqs. (1) and (2) using a finite volume formulation on a generalized curvilinear coordinate nonstaggered grid with a rigid lid. This code has been extensively validated with a number of different studies on geophysical fluid dynamics using its single-processor version (Zang and Street,<sup>26</sup> Zedler and Street,<sup>27</sup> Fringer and Street<sup>24</sup>) as well as its parallel version (Cui and Street<sup>28,29</sup>).

For all the simulations, the initial stratification is given by the background distribution  $\rho_b(z)$ , which is linear and is given by

$$\frac{\rho(z, t=0)}{\rho_0} - 1 = \frac{\rho_b(z)}{\rho_0} = -\frac{\Delta\rho}{\rho_0} \left( \frac{z}{d} \right), \quad (3)$$

with  $\Delta\rho/\rho_0=0.02$ , which results in a buoyancy frequency of  $N=0.57$  rad  $s^{-1}$  in a depth of  $d=60$  cm. At the left boundary of the domain shown in Fig. 1, we impose a first-mode internal wave given by

$$u(0, z, t) = U_0 \cos(mz) \sin(\omega t), \quad (4)$$

where  $U_0$  is the velocity amplitude of the forcing,  $m$  is the vertical wavenumber corresponding to a mode-1 baroclinic wave with  $m=\pi/d$ ,  $\omega$  is the forcing frequency, and  $u$  is the cross-shore velocity component. Boundary conditions for the cross-shore (horizontal) velocity  $u$  are no-slip on the bottom boundary, free-slip at the top boundary, and no-flux at the right boundary. The vertical velocity has a no-flux boundary condition at both top and bottom boundaries, and free-slip boundary conditions on all other walls, and the density field has a gradient-free boundary condition on all walls. The boundary condition given in Eq. (4) does not allow reflected waves at the left boundary to radiate out of the domain. Therefore, the simulations are halted before reflected waves from the boundary reach the slope. The grid size is  $512 \times 128$ , with a maximum Courant number of 0.2. We use a kinematic viscosity of  $\nu=10^{-5}$   $m^2 s^{-1}$  and a thermal diffusiv-

TABLE I. List of simulations performed showing the parameter space covered.  $\lambda_h = \pi/k$ ,  $T = 2\pi/\omega$ .

Runs	$\gamma/s$	$\text{Fr} = U_0/c_{\text{ph}}$	$U_0 T / (\pi L_s)$	$L_s/\lambda_h$	$(d-d_s)/d$	Comments
1–8	0	0.06–0.78	–	–	–	No-slope cases
9–18	0.25–1.5	0.06	0.05	0.7	0.17–0.72	Linear cases
19–28	0.25–1.5	0.45	0.41	0.7	0.17–0.72	Nonlinear cases
29–38	0.25–1.5	0.78	0.71	0.7	0.17–0.72	Highly nonlinear cases
39–46	1	0.06–0.78	0.05–0.71	0.7	0.57	Effects of nonlinearity
47–53	0.5	0.45	0.41	0.7–1.4	0.33–0.66	Effects of slope lengthscale

ity of  $\kappa = 10^{-6} \text{ m}^2 \text{ s}^{-1}$ , which gives a Prandtl number of  $\text{Pr} = 10$ . A rough estimate of the turbulent Reynolds number for these flows, based on the largest turbulent overturning length scale of  $L_c = 5 \text{ cm}$  and a characteristic overturning velocity of  $U_0 = 4 \text{ cm s}^{-1}$ , is  $\text{Re}_T = 200$ . The corresponding Kolmogorov microscale is then  $\eta_k = L_c \text{Re}_T^{-3/4} = 0.94 \text{ mm}$ . With a longitudinal grid spacing of  $15.6 \text{ mm}$  and vertical grid spacings of  $4.7 \text{ mm}$  in the deep region and  $1.6 \text{ mm}$  in the shallow region, the longitudinal grid spacing is about 15 times larger than the Kolmogorov microscale and the largest vertical grid spacing is 5 times larger.

### III. ENERGETICS

Internal wave modes propagate horizontally because they represent a superposition of phase-locked upward and downward propagating internal wave beams, which are characterized by both horizontal and vertical wavenumbers  $k$  and  $m$ . Upon encountering topography, the upward and downward propagating beams decouple and the dynamics is governed by the interaction of the beams with the topography. With respect to beamlike propagation of internal waves, bottom slopes are readily classified by the ratio  $\gamma/s$  (Phillips<sup>15</sup>), where  $\gamma$  is the bathymetric slope and  $s$  is the slope of the internal wave energy characteristic, which is defined by

$$s = \tan \theta = \frac{k}{m} = \left( \frac{\omega^2 - f^2}{N^2 - \omega^2} \right)^{1/2}, \quad (5)$$

where  $\theta$  is the angle of the internal wave characteristic,  $\omega$  is the wave frequency,  $f$  is twice the sine of latitude Coriolis parameter, and  $N$  is the buoyancy frequency. Supercritical slopes ( $\gamma/s > 1$ ) correspond to topographic slopes that are steeper than the wave characteristic slope, while subcritical slopes ( $\gamma/s < 1$ ) correspond to topographic slopes that are flat compared to the wave characteristic slope. Critical slopes ( $\gamma/s = 1$ ) correspond to waves in which the angle of propagation of the group velocity matches the topographic slope.

Linear first-mode internal waves in a uniformly stratified fluid propagate horizontally at the first-mode internal wave speed of (Kundu<sup>30</sup>)

$$c_{\text{ph}} = \frac{\omega}{k} = \frac{d}{\pi} (N^2 - \omega^2)^{1/2}, \quad (6)$$

where  $d$  is the water depth. While holding  $N$  and  $\omega$ , and hence  $s$ , fixed, we carried out a series of simulations with different topographic slopes  $\gamma$ , such that  $\gamma/s$  was varied from 0 to 1.5 and covered a broad range of sub- and supercritical

slopes. In this study, the topographic slope variation is achieved by changing the topographic amplitude given by  $(d-d_s)/d$ . We believe there is no unique way to obtain different values of  $\gamma/s$  without altering either  $(d-d_s)/d$  or changing the frequency of the incoming wave field (which would imply changing the incoming wave properties). We also varied the velocity amplitude  $U_0$  between  $0.5$  and  $7 \text{ cm s}^{-1}$ , in order to vary the Froude number ( $\text{Fr} = U_0/c_{\text{ph}}$ ), which ranged from  $0.056$  to  $0.783$ . This yielded a parameter space that allowed us to assess the energy flux distributions for a wide range of conditions spanning from linear waves up to conditions where nonlinear wave effects are strong. Table I lists the parameter space covered by the simulations.

#### A. Density and velocity fields

Figure 2 depicts the density contours (isopycnals) for the critical case ( $\gamma/s = 1$ ) obtained by imposing a first-mode internal wave field at the left boundary of the domain shown in Fig. 1 using Eq. (4). Three cases with  $\text{Fr} = 0.056$ ,  $0.447$ , and  $0.783$  are shown in this figure, corresponding to linear, nonlinear, and highly nonlinear waves, respectively, and the frequency of the incoming wave is  $\omega = 0.33 \text{ rad s}^{-1}$  for all three cases. This figure shows results at six points in time normalized by the linear wave period  $T = 2\pi/\omega$  for the right half of the domain starting at  $x = 4.5 \text{ m}$ . For the linear case [Fig. 2(a)], the isopycnal displacements are very small. For the nonlinear and highly nonlinear cases [Figs. 2(b) and 2(c)], the sequence depicts wave breaking and the formation of up-slope surging bores that are ejected onto the shelf as propagating internal boluses. For these high-Fr cases, the incoming waves are large-scale features with amplitudes of the order of half the depth of the water column and are indicative of the features of the waves observed in the field by Petruccio *et al.*<sup>31</sup>

Figures 3 and 4 show the horizontal velocity, vertical velocity and density profiles at sections A-A (off-shelf) and B-B (on-shelf) shown in Fig. 2 for the linear and highly nonlinear cases, respectively, at time  $t/T = 5.9$ . The velocity profiles for the linear case [Figs. 3(a), 3(b), 4(a), and 4(b)] show that the incoming wave field propagates as low-internal modes both on- and off-shelf, with the stratification remaining relatively unaltered [Figs. 3(c) and 4(c)]. On the other hand, the velocity profiles for the nonlinear cases [Figs. 3(d), 3(e), 4(d), and 4(e)] indicate significant departures from the mode-1 modal structure, indicating the generation of higher modes as a result of the interaction with the topography. In

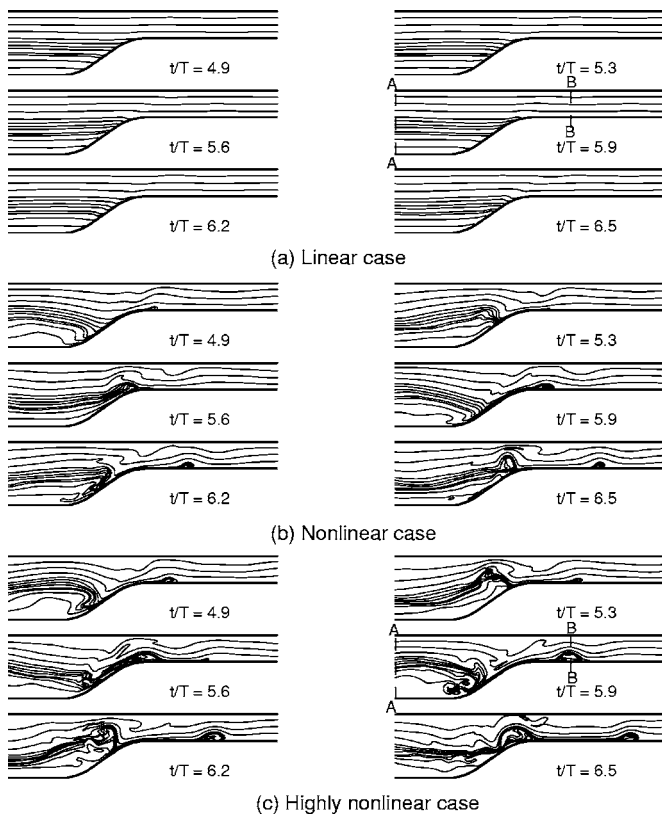


FIG. 2. Density contours of an internal wave interacting with a critical slope for (a) a linear case with  $Fr=0.056$ , (b) a nonlinear case with  $Fr=0.447$ , and (c) a highly nonlinear case with  $Fr=0.783$ . Both the nonlinear and highly nonlinear cases show how the internal bolus propagates onshore as a result of the interaction process [see Fig. 5 for a detail of the bolus core shown in (c)]. Contours of density are plotted every 0.2%.

particular, the density profile on-shelf [Fig. 4(f)] reveals the presence of dense offshore water that is transported by the on-shelf propagating internal boluses. These internal boluses seen on the shelf are analogous to the nonlinear waves of elevation observed by Carter *et al.*<sup>11</sup> and Klymak and Moum<sup>8</sup> in Monterey Bay and off the Oregon Coast, respectively. The

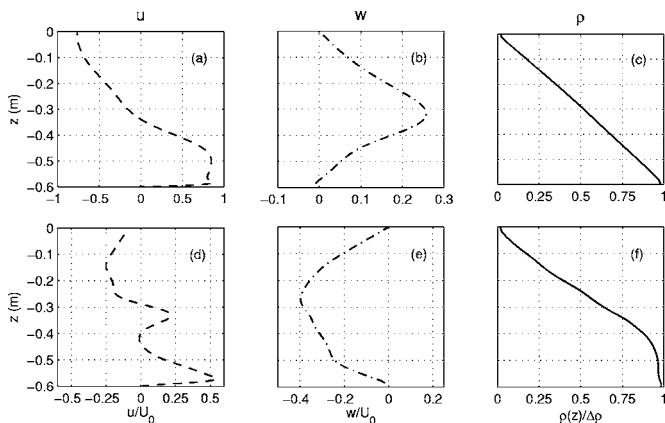


FIG. 3. Velocity and density profiles at section A-A at  $t/T=5.9$ , for the linear (a)–(c) and highly nonlinear (d)–(f) cases shown in Fig. 2. The velocities are normalized by the velocity amplitudes of  $U_0=0.005$  and  $0.07 \text{ m s}^{-1}$  corresponding to the linear and highly nonlinear cases, respectively, while the density profiles are normalized by the density difference of  $\Delta\rho=20 \text{ kg m}^{-3}$ .

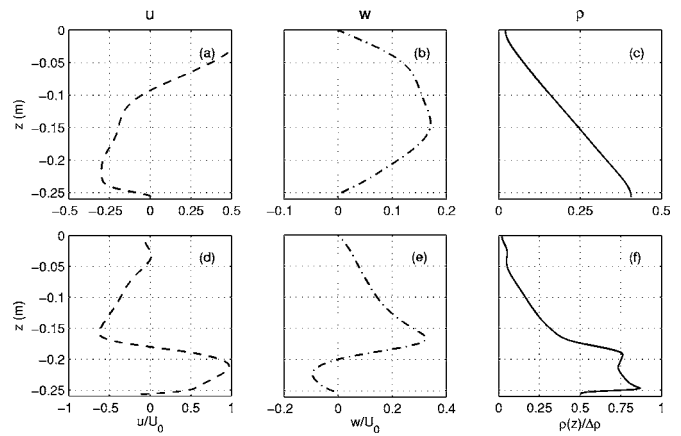


FIG. 4. Velocity and density profiles at section B-B at  $t/T=5.9$ , for the linear (a)–(c) and highly nonlinear (d)–(f) cases shown in Fig. 2. The velocities are normalized by the velocity amplitudes of  $U_0=0.005$  and  $0.07 \text{ m s}^{-1}$ , corresponding to the linear and highly nonlinear cases, respectively, while the density profiles are normalized by the density difference of  $\Delta\rho=20 \text{ kg m}^{-3}$ .

passage of these boluses displaces isopycnals locally and can provide significant bursts of turbulent kinetic energy that can contribute to diapycnal mixing and sediment resuspension. The boluses have large onshore velocities contained within their well-mixed cores as shown in Fig. 5, which depicts a detail of the internal bolus shown in Fig. 2(c) at  $t/T=5.9$ . The onshore propagation speed of these boluses coupled with the circulation within their cores leads to large near-bed velocities making these signatures prime candidates for entraining and transporting mass.

**B. Energy flux**

The equation governing the energetics of NLIWs is obtained by taking the dot product of equation (1) with  $\mathbf{u}$  and multiplying equation (2) by  $gz$  and adding the two resulting equations to obtain

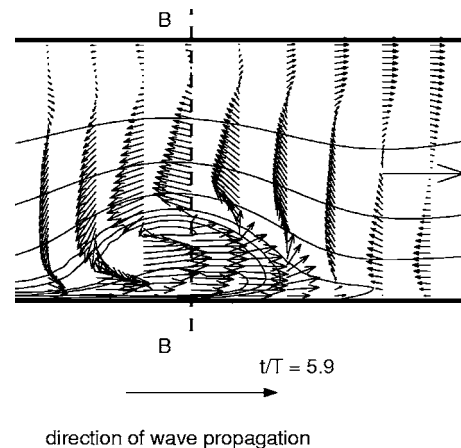


FIG. 5. Velocity vectors superimposed on the density contours to show the amplification of onshore velocities within the boluses. This figure is a blown-up detail of the bolus shown in Fig. 2(c) at time  $t/T=5.9$ . The magnitude of the single horizontal velocity vector in the right-hand center of the figure is  $10 \text{ cm s}^{-1}$ . Waves propagate from left to right.

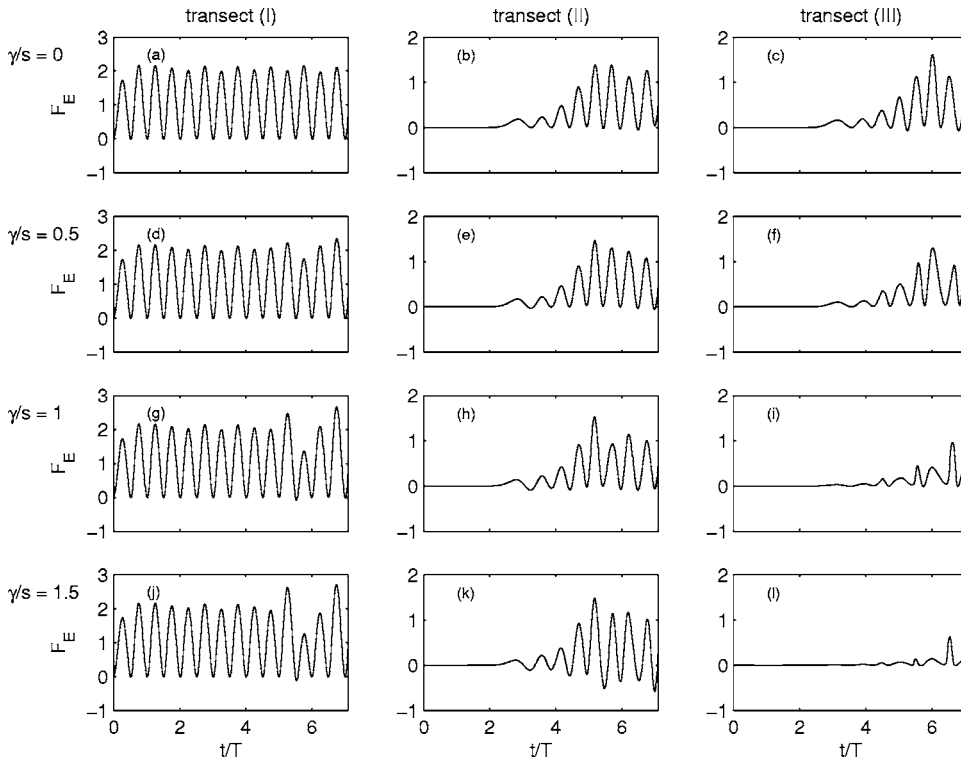


FIG. 6. Normalized energy fluxes  $F_E$  as function of time  $t/T$  at transects (I), (II), and (III) shown in Fig. 1, for  $\gamma/s=0$  (no-slope case);  $\gamma/s=0.5$  (subcritical slope);  $\gamma/s=1$  (critical slope), and  $\gamma/s=1.5$  (supercritical slope);  $T = 19.2$  s,  $Fr = U_0/c_{ph} = 0.447$ .

$$\frac{\partial}{\partial t}(\rho_0 q + \rho g z) + \nabla \cdot \mathbf{f} = -\rho_0 \epsilon_k - 2\kappa \frac{\partial}{\partial z}(\rho g), \quad (7)$$

where  $q = \mathbf{u} \cdot \mathbf{u}/2$  is the kinetic energy per unit mass,  $\epsilon_k$  is the viscous dissipation rate of kinetic energy and is given by  $\epsilon_k = \nu \partial u_i / \partial x_j \partial u_j / \partial x_i$ , and the local energy flux is given by

$$\mathbf{f} = \mathbf{u}(\rho_0 q + p + \rho g z) - \mu \nabla q - \kappa \nabla(\rho g z). \quad (8)$$

Here,  $\mu$  is the dynamic viscosity. Integrating Eq. (7) in time from  $t=0$  to  $6.6T$ , and from sections II to III in Fig. 1 and over the depth gives

$$\Delta E_\tau + (E_\tau)_{\text{III}} - (E_\tau)_{\text{II}} = -\epsilon + \phi_i, \quad (9)$$

where, in units of  $\text{J m}^{-1}$ , the change in total energy within the control volume is given by

$$\Delta E_\tau = \int_0^{L_2} \int_{-d}^0 [\rho_0 q + g(\rho - \rho_b)z] dz dx, \quad (10)$$

and, in units of  $\text{J m}^{-1}$ , the time-integrated energy flux is given by

$$E_\tau = \int_0^t F_E(\tau) d\tau, \quad (11)$$

where, in units of  $\text{W m}^{-1}$ , the depth-integrated energy flux is given by

$$F_E = \int_{-d}^0 \left[ u(\rho_0 q + \rho g z + p) - \mu \frac{\partial q}{\partial x} - \kappa \frac{\partial}{\partial x}(\rho g z) \right] dz. \quad (12)$$

In Eq. (9),  $\epsilon$  is the integrated kinetic energy dissipation, and  $\phi_i$  is the time-integrated energy flux through the upper and lower surfaces, i.e.,  $\phi_i = -2\kappa g \int_0^{L_2} \int_0^{L_2} (\rho_{\text{top}} - \rho_{\text{bottom}}) dx d\tau$  (as defined in Winters *et al.*<sup>32</sup>), and the change in the total energy is

computed by assuming that at  $t=0$ , the density field is given by the background density field  $\rho_b$ . To a good approximation, the contribution of the diffusive terms to the energy flux is negligible, and the depth-integrated energy flux reduces to

$$F_E = \int_{-d}^0 p' u dz, \quad (13)$$

where  $p' = \rho_0 q + \rho g z + p$ . Splitting the pressure  $p$  into its hydrostatic ( $P_H$ ) and nonhydrostatic ( $P_{NH}$ ), components then gives  $p' = \rho_0 q + \rho g z + p_H + p_{NH}$ . Roughly 50% of the energy flux is due to the density field, while 30% is due to the nonhydrostatic pressure. A detailed analysis of the different terms can be found in the work of Venayagamoorthy and Fringer.<sup>33</sup>

Figure 6 shows the depth-integrated energy flux from equation (13) as a function of time at locations (I), (II), and (III) shown in Figure 1. Transects (II) and (III) represent cross sections at the beginning and end of the shelf break and define the edges of the control volume over which the analysis in this study is performed. Results are shown for four different ratios of slope angle to beam propagation angle, i.e.,  $\gamma/s=0, 0.5, 1$  and  $1.5$ , depicting no-slope, subcritical, critical, and supercritical slopes, respectively, and the Froude number is fixed at  $Fr=0.447$ . All the fluxes have been normalized by the estimate of energy flux of an incoming internal wave using linear theory (Kundu<sup>30</sup>), for which

$$F_L = \frac{\rho_0 \omega U_0^2}{2k} d, \quad (14)$$

where  $\rho_0$  is the reference density,  $\omega$  is the forcing frequency,  $U_0$  is the forcing amplitude,  $d$  is the offshore depth,  $m = \pi/d$  is the vertical wavenumber, and  $k$  is the horizontal

wavenumber that is readily obtained from the dispersion relation for internal waves. The energy flux  $F_L$  given by Eq. (14) is simply the integral of the product of the velocity and pressure perturbations. Using the definition for the slope of an internal wave group velocity characteristic from Eq. (5), after some manipulation it is easy to show that, in the absence of rotation ( $f=0$ ),

$$\frac{F_L}{\rho_0} = \frac{1}{2} U_0^2 c_1 d \frac{1}{(1+s^2)^{1/2}}, \quad (15)$$

where  $c_1$  is the mode-1 baroclinic wave speed for a linear hydrostatic ( $\omega \ll N$ ) internal wave and can be deduced from Eq. (6) to be  $Nd/\pi$ . Equation (15) can then be put in nondimensional form as

$$\frac{F_L}{F_0} = \frac{Fr_h^2}{(1+s^2)^{1/2}}, \quad (16)$$

where  $F_0 = \frac{1}{2} \rho_0 c_1^3 d$  is constant for all the simulations, and  $Fr_h = U_0/c_1$  is also a Froude number based on the hydrostatic linear wave speed  $c_1$ . Equation (16) implies that the incident linear energy flux grows quadratically with the Froude number for a given wave group velocity slope  $s$ . On the other hand, for a given Froude number, the energy flux should decrease with increasing wave slope  $s$ .

The lower peaks in the energy fluxes at transect (I) in Figs. 6(d), 6(g), and 6(j), signify the arrival of wave energy at the left boundary, which has reflected from the slope. As noted previously, the reflected energy does not radiate but instead reflects back towards the slope. As a result, we halt the simulations before this re-reflected energy contaminates the energetics of interest. At transect (II) [Figs. 6(e), 6(h), and 6(k)], the computed energy fluxes include both the incident energy flux coming from the waves approaching the slope as well as wave energy flux that is reflected offshore from the slope. Hence, they provide a measure of the combined energy flux from incident and reflected waves; i.e.,  $F_{E,i} + F_{E,r}$ . In order to extract the reflected portion of the energy flux at transect (II), we use the energy flux computed at the same location for the no-slope case ( $\gamma/s=0$ ) shown in Fig. 6(b). This provides a measure of the incident energy flux, i.e.,  $F_{E,i}$  for all the runs for a given  $Fr$ . The difference between  $F_{E,i}$  obtained from the no-slope case and the measured fluxes for any other case with  $\gamma/s > 0$  is the amount of reflected energy flux ( $F_{E,r}$ ) from the slope for that particular case. The transmitted (or forward-reflected) energy fluxes ( $F_{E,t}$ ) are shown in Figs. 6(c), 6(f), 6(i), and 6(l). The transmitted energy fluxes decrease significantly as  $\gamma/s$  increases due to increased reflection away from the slope as seen, for example, in Fig. 6(k) for  $\gamma/s=1.5$ . We find that as  $Fr$  increases, the instantaneous energy fluxes that reach the shelf for the near-critical slopes and beyond become intermittent and occur due to the passage of the energetic internal boluses.

Figure 7 shows the cumulative (time-integrated) horizontal energy flux given in Eq. (11) normalized by  $F_L/\omega$  for the cases shown in Fig. 6. The effects of the reflection from

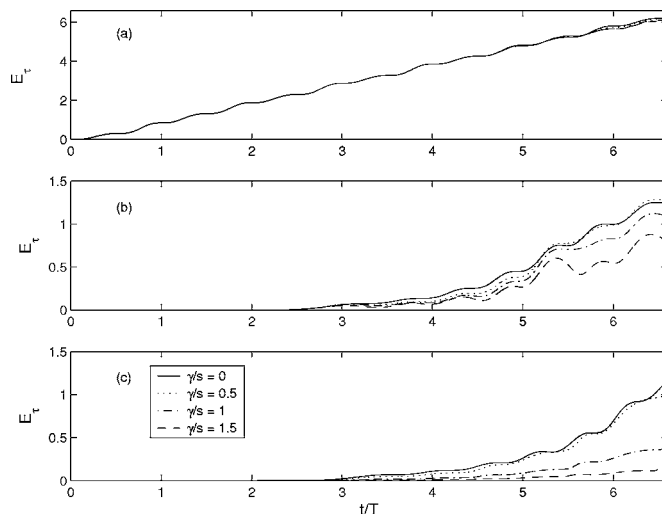


FIG. 7. Normalized cumulative energy fluxes  $E_\tau$  as function of time  $t/T$  at transects (I), (II), and (III) shown in Fig. 1. Solid lines:  $\gamma/s=0$  (no-slope case); dotted lines:  $\gamma/s=0.5$  (subcritical slope); dash-dotted:  $\gamma/s=1$  (critical slope); dashed lines:  $\gamma/s=1.5$  (supercritical slope);  $T=19.2$  s;  $Fr=U_0/c_{ph}=0.447$ .

the slope for steeper topographic slopes are clearly evident in the reduced cumulative fluxes as shown in Figs. 7(b) and 7(c).

From Eq. (9), if we neglect the contribution of  $\phi_i$  (Fringer<sup>34</sup>), then the energy budget can be approximated by

$$E_I = E_R + E_T + E_D, \quad (17)$$

where, as depicted in the schematics shown in Fig. 8, the cumulative incident energy is  $E_I = (E_\tau)_{II,ns}$ , the cumulative reflected energy is  $E_R = (E_\tau)_{II,ns} - (E_\tau)_{II,ws}$ , and the cumulative transmitted energy is  $E_T = (E_\tau)_{III,ws}$ , and  $E_D = (\epsilon + \Delta E_\tau)_{ws}$  is the energy change in the control volume due to mixing and dissipation, where  $\epsilon$  is the integrated dissipation and  $\Delta E_\tau$  is defined in Eq. (10).

An understanding of the dynamics of the transmission process can be gained by analyzing the ratio of transmitted to incident energy in the cumulative sense. In Fig. 9, we show the results of the cumulative transmitted, reflected and dissipated energy fluxes for ten different values of  $\gamma/s$  and for three different values of the Froude number, i.e.,  $Fr=0.056$ ,  $0.447$ , and  $0.783$ , depicting linear, nonlinear, and highly nonlinear cases, respectively. For all  $Fr$ , the transmission ratio  $E_T/E_I$  drops monotonically with  $\gamma/s$  as shown in Fig. 9(a). For the linear case, most of the energy is transmitted for low values of  $\gamma/s$ , with the remaining energy dissipated on slope, while for near-critical and supercritical slopes, the ratio of reflected to incident energy  $E_R/E_I$  [Fig. 9(b)] increases as the topographic slope steepens and asymptotes to 1 in the inviscid limit as  $\gamma/s \rightarrow \infty$ , since we have chosen the slope length  $L_s$  to be equal to the offshore water depth  $d$ . These results corroborate well with linear theory. However, as  $Fr$  increases, some interesting trends emerge. First, the transmitted energy fluxes for subcritical slopes decrease with corresponding increases in dissipation as shown in Fig. 9(c), whereas the transmitted energy fluxes for the near-critical and supercritical slopes are slightly higher for the nonlinear

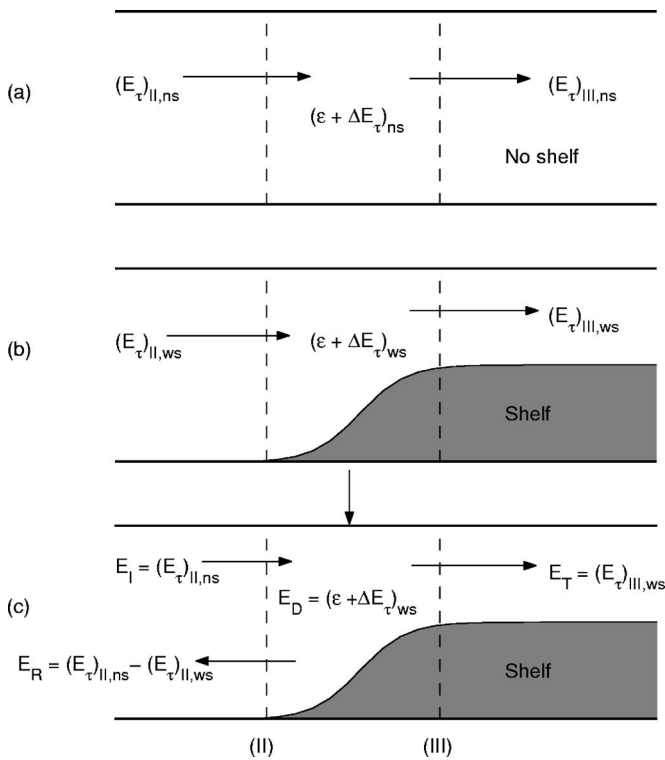


FIG. 8. Schematic of the energy budget for the control volume bounded by transects (II) and (III) in Fig. 1, where schematic (a) shows the no-slope case ( $\gamma/s=0$ ); schematic (b) shows a typical case with a shelf ( $\gamma/s>0$ ). Schematic (c) shows how the energy flux budget is closed by using schematics (a) and (b) to obtain the incident and reflected energy fluxes; i.e.,  $E_I$  and  $E_R$ , respectively. The subscript *ns* implies “no-slope,” while the subscript *ws* implies “with-slope.”

case ( $Fr=0.447$ ) than for the linear case ( $Fr=0.056$ ). This suggests that there is an optimum Froude number that maximizes the transmission of the energy flux. Second, the reflected energy fluxes for the near-critical and supercritical slopes are suppressed monotonically with increasing  $Fr$  as shown in Fig. 9(b). This loss can be attributed to the more vigorous nature of the interaction of the large-amplitude incoming waves with the slope, with a significant amount of the reflected energy being trapped within the slope region, leading to enhanced levels of dissipation and possible mixing. Overall, dissipation and mixing on the slope is enhanced significantly as  $Fr$  increases with peak dissipation occurring for the critical slope due to the intense focusing of wave energy on-slope, while reflection is attenuated. The transmission rates for supercritical slopes are sustained mainly through the highly energetic and intermittent bursts of energy on-shelf brought about by the passage of the internal boluses that form as a result of the nonlinear interaction with the slope.

To investigate further the optimum level of nonlinearity for a given value of  $\gamma/s$  in the near-critical region, we ran simulations with more values of  $Fr$  that cover the gaps in the data represented in Fig. 9 for the critical slope. Figure 10 shows the ratio of cumulative transmitted to incident energy flux as a function of  $Fr$  for  $\gamma/s=1$ . Our results show almost a plateau in the transmission ratios for  $Fr$  in the range of 0.22 to 0.45 with a slight peak occurring at  $Fr=0.34$ . We also plot

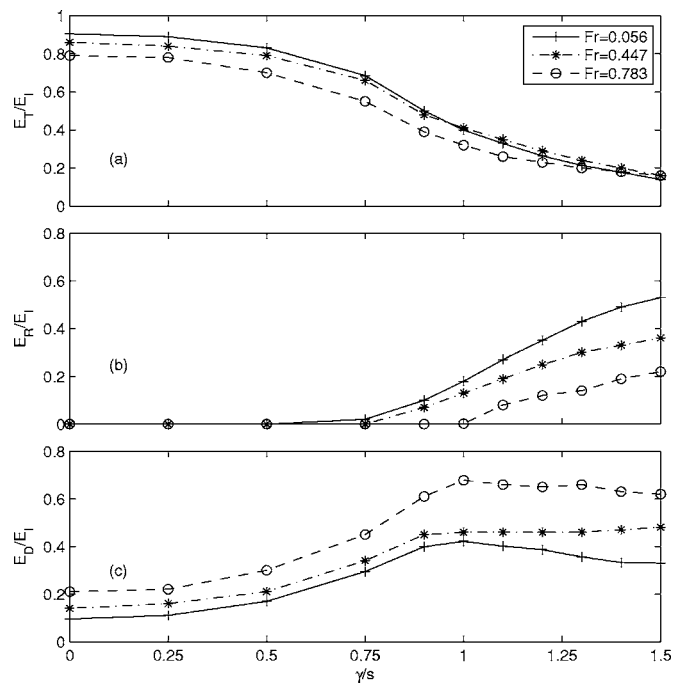


FIG. 9. Cumulative energy fluxes normalized by the cumulative incident energy flux  $E_i$ , as a function of topographic steepness: (a) cumulative transmitted energy fluxes; (b) cumulative reflected energy fluxes; (c) cumulative dissipation and mixing. Solid lines: linear case with  $Fr=0.056$ ; dashed-dotted lines: nonlinear case with  $Fr=0.447$ ; dashed lines: highly nonlinear case with  $Fr=0.783$ .

the transmission ratio as a function of the parameter  $Fr_E = U_0 T / (\pi L_s)$ , which gives a measure of the particle excursion over half the wave period  $T$  normalized by the topographic lengthscale  $L_s$ . The corresponding values of  $Fr_E$  where the plateau in the transmission occurs are in the range 0.2–0.4. It is plausible to suggest that there is a range of optimum level of nonlinearity where the transmission is maximum for slopes that are in the near-critical region. The peak transmission occurs as a result of the interaction of the wave field with the slope in such a way that tends to maximize the up-slope surge of fluid onto the shelf for an optimum degree of nonlinearity, beyond which dissipation and mixing overwhelm the dynamics. This alludes to the need for three-dimensional simulations in order gain a more detailed understanding of the interaction dynamics on the slope.

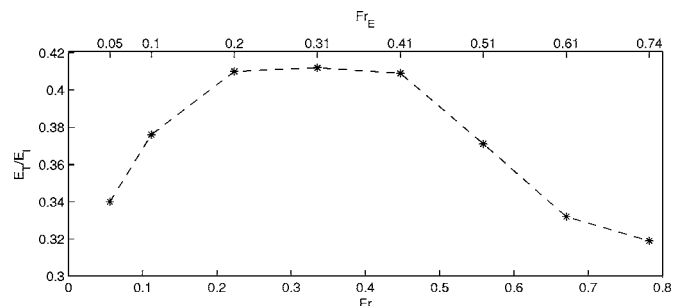


FIG. 10. Cumulative transmitted energy flux as a function of Froude numbers, i.e.,  $Fr=U_0/c_{ph}$  (bottom  $x$  axis) and  $Fr_E=U_0 T / (\pi L_s)$  (top  $x$  axis), for critical slope ( $\gamma/s=1$ ).

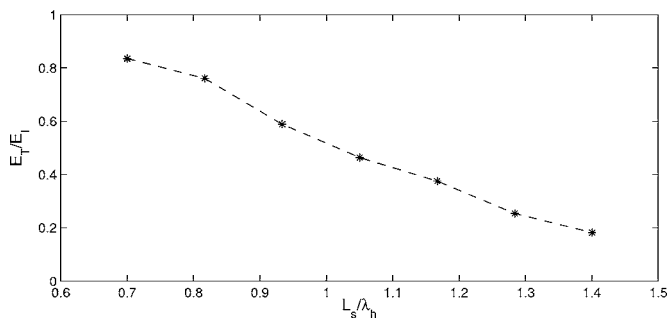


FIG. 11. Cumulative transmitted energy flux as a function of topographic scale  $L_s/\lambda_h$  for a subcritical slope  $\gamma/s=0.5$  and Froude number  $Fr=0.447$ .

For the main set of runs we have discussed, we held the slope length  $L_s$  constant. However, another important parameter that will influence the energetics is the ratio of the topographic lengthscale  $L_s$  to the half-wavelength  $\lambda_h$  of the incoming wave for any given topographic slope  $\gamma$ . Due to the computational costs involved in investigating the entire parameter space resulting from the need for increased domain sizes that have to be computed, we restricted our investigation of the ratio  $L_s/\lambda_h$  to single values of  $\gamma/s=0.5$  and  $Fr=0.447$ . With the same incoming wave with a frequency of  $\omega=0.33 \text{ rad s}^{-1}$ , we varied the slope length  $L_s$  from 0.6 to 1.2 m in increments of 0.1 m, which yielded values of  $L_s/\lambda_h$  in the range 0.7–1.4. The results of the cumulative transmitted energy flux normalized by the cumulative incident energy flux  $E_T$ , as a function of  $L_s/\lambda_h$  are shown in Fig. 11. The transmitted energy flux drops monotonically with increasing values of  $L_s/\lambda_h$ . This is indeed predictable since the relative excursion of the fluid particles will decrease as the topographic scale increases, which results in more on-slope dissipation.

#### IV. CONCLUSION

We have presented two-dimensional high-resolution simulations of internal waves interacting with a sloped coastal shelf break. The simulations described in this study have covered a range of wave amplitudes spanning from linear waves up to strongly nonlinear waves where internal boluses develop due to the complex interaction of the incoming wave with the topography.

As expected, for small-amplitude (low- $Fr$ ) waves, most of the energy is transmitted for subcritical (flat) topography ( $\gamma/s < 1$ ) and a large fraction of the energy is reflected for supercritical (steep) topography ( $\gamma/s > 1$ ). However, as nonlinearity increases, the transmission rates drop slightly from the linear case for subcritical slopes mainly due to corresponding increases in dissipation. On the other hand, for slopes close to critical and beyond, the transmission of energy does not differ much from its linear counterpart and in fact does increase slightly and then decreases as  $Fr$  increases. We hypothesize that this sustained transmission occurs due to the formation of the nonlinear internal boluses due to complex interaction of the incoming wave with the topography and subsequent propulsion of these dense vortex cores onto the shelf, providing significant intermittent bursts of

energy. The more profound impact is on the amount of reflected energy in the near-critical to supercritical regions. Here, nonlinearity drastically suppresses reflection in a monotonic way. This occurs due to more vigorous interaction of the wave field with the slope leading to the trapping of reflected waves within the slope region resulting in enhanced dissipation and mixing.

The calculations for varying Froude numbers for the critical slope indicate that there is an optimum degree of nonlinearity that tends to maximize transmission. Beyond the optimum Froude number, dissipation overwhelms both transmission and reflection. Furthermore, the instantaneous transmitted fluxes for the near-critical and supercritical slopes are highly intermittent and provide significant bursts of energy on-shelf. The internal boluses that transmit this energy provide an effective mechanism for transporting mass onshore and are a likely source of significant energy for diapycnal mixing on coastal shelves.

While the overall energetics are well-described by two-dimensional simulations, the mechanisms through which these nonlinear internal waves interact with the surrounding fluid are inherently three-dimensional. Further work is in progress to extend our calculations to three dimensions in order to obtain a better understanding of the turbulent dynamics, instabilities, mixing, and dissipation associated with these highly nonlinear waves and the discussion is left to a subsequent paper.

We note that application of the results reported here to real geophysical flows is limited by the low Reynolds number of the simulations. Therefore, one useful extension would be to expand the Reynolds number range of the simulations so as to clarify its influence on the interaction processes. For example, at higher Reynolds numbers, it is likely that the three-dimensionality will be especially important in the boundary layer as well as in the overturning regions.

#### ACKNOWLEDGMENTS

The authors wish to acknowledge the useful comments of two anonymous referees and we thank Jim Rottman for many helpful discussions and comments. We gratefully acknowledge the support of the Leavell Family Faculty Scholarship in the Department of Civil and Environmental Engineering at Stanford University and ONR Grant No. N00014-05-1-0294 (Scientific officers: Dr. C. Linwood Vincent, Dr. Terri Paluszkiwicz, and Dr. Scott Harper).

<sup>1</sup>W. Munk and C. Wunsch, "Abyssal recipes II: energetics of tidal and wind mixing," *Deep-Sea Res.* **45**, 1977 (1998).

<sup>2</sup>J. R. Ledwell, A. J. Watson, and C. S. Law, "Mixing of a tracer in the pycnocline," *J. Geophys. Res.* **10321**, 499 (1998).

<sup>3</sup>K. L. Polzin, J. M. Toole, J. R. Ledwell, and R. W. Schmitt, "Spatial variability of turbulent mixing in the abyssal ocean," *Science* **76**, 93 (1997).

<sup>4</sup>E. Kunze and J. M. Toole, "Tidally driven vorticity, diurnal shear, and turbulence atop fieberling seamount," *J. Phys. Oceanogr.* **27**, 2663 (1997).

<sup>5</sup>L. A. Ostrovsky and Y. A. Stepanyants, "Do internal solitons exist in the ocean?" *Rev. Geophys.* **27**, 293 (1989).

<sup>6</sup>J. R. Apel, J. R. Holbrook, A. K. Liu, and J. J. Tsai, "The Sulu Sea internal soliton experiment," *J. Phys. Oceanogr.* **15**, 1625 (1985).

<sup>7</sup>H. Sandstrom and N. S. Oakey, "Dissipation in internal tides and solitary waves," *J. Phys. Oceanogr.* **25**, 604 (1995).

<sup>8</sup>J. M. Klymak and J. N. Moum, "Internal solitary waves of elevation

- advancing on a shoaling shelf," *Geophys. Res. Lett.* **30**, 2045 (2003).
- <sup>9</sup>P. Hosegood, J. Bonnin, and H. van Haren, "Solibore-induced sediment resuspension in the Faeroe-Shetland Channel," *Geophys. Res. Lett.* **31**, L09301 (2004).
- <sup>10</sup>A. Scotti and J. Pineda, "Observations of very large and steep internal waves of elevation near the Massachusetts coast," *Geophys. Res. Lett.* **31**, L22307 (2004).
- <sup>11</sup>G. S. Carter, M. C. Gregg, and R.-C. Lien, "Internal waves, solitary waves, and mixing on the Monterey Bay shelf," *Cont. Shelf Res.* **25**, 1499 (2005).
- <sup>12</sup>V. Vlasenko and K. Hutter, "Numerical experiments on the breaking of solitary internal waves over a slope-shelf topography," *J. Phys. Oceanogr.* **32**, 1779 (2002).
- <sup>13</sup>S. A. Thorpe, "On the reflection of a strain of finite-amplitude internal waves from a uniform slope," *J. Fluid Mech.* **178**, 279 (1987).
- <sup>14</sup>T. Dauxois and W. R. Young, "Near-critical reflection of internal waves," *J. Fluid Mech.* **390**, 271 (1999).
- <sup>15</sup>O. M. Phillips, *The Dynamics of the Upper Ocean* (Cambridge University Press, Cambridge, 1977).
- <sup>16</sup>D. N. Slinn and J. J. Riley, "Turbulent dynamics of a critically reflecting internal gravity wave," *Theor. Comput. Fluid Dyn.* **11**, 281 (1998).
- <sup>17</sup>A. Javam, J. Imberger, and S. W. Armfield, "Numerical study of internal wave reflection from sloping boundaries," *J. Fluid Mech.* **396**, 183 (1999).
- <sup>18</sup>D. Cacchione and C. Wunsch, "Experimental study of internal waves over a slope," *J. Fluid Mech.* **66**, 223 (1974).
- <sup>19</sup>G. N. Ivey and R. I. Nokes, "Vertical mixing due to the breaking of critical internal waves on sloping boundaries," *J. Fluid Mech.* **204**, 479 (1989).
- <sup>20</sup>G. N. Ivey, K. B. Winters, and I. P. D. De Silva, "Turbulent mixing in a sloping benthic boundary layer energized by internal waves," *J. Fluid Mech.* **418**, 59 (2000).
- <sup>21</sup>S. Legg and A. Adcroft, "Internal wave breaking at concave and convex continental slopes," *J. Phys. Oceanogr.* **33**, 2224 (2003).
- <sup>22</sup>T. P. Stanton and L. A. Ostrovsky, "Observations of highly nonlinear internal solitons over the continental shelf," *Geophys. Res. Lett.* **25**, 2695 (1998).
- <sup>23</sup>P. D. Craig, "Internal wave dynamics over coastal topography," Ph.D thesis, University of Western Australia, 1985.
- <sup>24</sup>O. B. Fringer and R. L. Street, "The dynamics of breaking progressive interfacial waves," *J. Fluid Mech.* **494**, 319 (2003).
- <sup>25</sup>Y. Zang, R. L. Street, and J. R. Koseff, "A non-staggered grid, fractional step method for time-dependent incompressible Navier-Stokes equations in curvilinear coordinates," *J. Comput. Phys.* **114**, 18 (1994).
- <sup>26</sup>Y. Zang and R. L. Street, "Numerical simulation of coastal upwelling and interfacial instability of a rotating stratified fluid," *J. Fluid Mech.* **305**, 47 (1995).
- <sup>27</sup>E. A. Zedler and R. L. Street, "Large-eddy simulation of sediment transport: Currents over ripples," *J. Hydraul. Eng.* **127**, 444 (2001).
- <sup>28</sup>A. Cui and R. L. Street, "Large-eddy simulation of turbulent rotating convective flow development," *J. Fluid Mech.* **447**, 53 (2001).
- <sup>29</sup>A. Cui and R. L. Street, "Large-eddy simulation of coastal upwelling flow," *Environ. Fluid Mech.* **4**, 197 (2004).
- <sup>30</sup>P. K. Kundu, *Fluid Mechanics* (Academic, London, 1990).
- <sup>31</sup>E. T. Petrucio, L. K. Rosenfeld, and J. D. Paduan, "Observations of the internal tide in Monterey Canyon," *J. Phys. Oceanogr.* **28**, 1873 (1998).
- <sup>32</sup>K. B. Winters, P. N. Lombard, J. J. Riley, and E. A. D'Asaro, "Available potential energy and mixing in density-stratified flows," *J. Fluid Mech.* **289**, 115 (1995).
- <sup>33</sup>S. K. Venayagamoorthy and O. B. Fringer, "Nonhydrostatic and nonlinear contributions to the energy flux budget in nonlinear internal waves," *Geophys. Res. Lett.* **32**, L15603 (2005).
- <sup>34</sup>O. B. Fringer, "Numerical simulations of breaking interfacial waves," PhD thesis, Stanford University (2001).